

Anisotropy and microcrack-induced failure precursor of shales under dynamic splitting

Xianhui Feng, Bin Gong, Xiaofeng Cheng, Huihui Zhang & Chun'an Tang

To cite this article: Xianhui Feng, Bin Gong, Xiaofeng Cheng, Huihui Zhang & Chun'an Tang (2022) Anisotropy and microcrack-induced failure precursor of shales under dynamic splitting, *Geomatics, Natural Hazards and Risk*, 13:1, 2864-2889, DOI: [10.1080/19475705.2022.2137440](https://doi.org/10.1080/19475705.2022.2137440)

To link to this article: <https://doi.org/10.1080/19475705.2022.2137440>



© 2022 The Author(s). Published by Informa UK Limited, trading as Taylor & Francis Group.



Published online: 30 Oct 2022.



Submit your article to this journal [↗](#)



Article views: 84





View related articles [↗](#)



View Crossmark data [↗](#)

Anisotropy and microcrack-induced failure precursor of shales under dynamic splitting

Xianhui Feng^a , Bin Gong^b , Xiaofeng Cheng^a, Huihui Zhang^a and Chun'an Tang^a

^aState Key Laboratory of Coastal & Offshore Engineering, Dalian University of Technology, Dalian, China; ^bDepartment of Civil and Environmental Engineering, Brunel University London, London, UK

ABSTRACT

The dynamic anisotropy and failure mechanism of shales are greatly affected by bedding surfaces. To reveal the influence of beddings on anisotropic characteristics of shales under dynamic impact, the Brazilian splitting tests were conducted by the split Hopkinson pressure bar system. The fracturing process were monitored by the high-speed camera. Meanwhile, to understand crack initiation and propagation mechanism, the stress buildup, stress shadow and stress transfer were modelled based on the digital image processing and the rock failure process analysis method. The effect of dip angle and bedding spacing on crack initiation, propagation and coalescence was analyzed. Simultaneously, the spatial distribution and energy magnitude of crack-induced acoustic emissions were captured numerically. The results show that the shale discs continue to produce parallel cracks and cambered cracks induced by the high stresses at the tips of initial cracks; the tensile strength under dynamic splitting changes in the U-shaped trend with the bedding dip angle increasing; the cracking percentage of bedding surfaces decreases, and the cracking percentage of rock matrix increases with the bedding dip angle increasing. In addition, the acceleration of crack growth and the rapid growth of AE energy can be regarded as the effective precursors of shale failure.

ARTICLE HISTORY

Received 29 August 2022
Accepted 13 October 2022

KEYWORDS

Dynamic anisotropy; split Hopkinson pressure bar; Brazilian splitting; bedded shale; acoustic emission precursor

1. Introduction

The stability and safety of rock masses is greatly influenced by the naturally existing discontinuities. Shales containing bedding surfaces are widely distributed on the Earth and are often encountered during slope excavation, tunnelling, mining, *etc.* (Xu et al. 2019; Zhang et al. 2019; Li et al. 2020; Yu et al. 2020). Under the geological processes of weathering, transportation and sedimentation, many shales are featured by the distinctive bedding structure (Zhang et al. 2018). Because of the significant differences

CONTACT Bin Gong  bin.gong@brunel.ac.uk

© 2022 The Author(s). Published by Informa UK Limited, trading as Taylor & Francis Group.

This is an Open Access article distributed under the terms of the Creative Commons Attribution License (<http://creativecommons.org/licenses/by/4.0/>), which permits unrestricted use, distribution, and reproduction in any medium, provided the original work is properly cited.

between the mechanical properties of bedding planes and rock matrix, shales usually show strong anisotropy under the action of dynamic impact, which may lead to the uneven deformation and unexpected failure of engineered rock masses and threaten the safety of life and property (Ma et al. 2017; Zhang et al. 2017; Wang et al. 2020a). Actually, the dynamic anisotropy has a substantial influence on various strength and deformation properties of shales (Khanlari et al. 2014; Wang et al. 2016; Suo et al. 2020) depending on the structural characteristics and load/unload directions (Eliyahu et al. 2015; Haeri et al. 2018). On the one hand, shale matrix is relatively heterogeneous and micro-cracks may generate at the pre-existing defects, such as voids, grain boundaries, inclusions, *etc.*, under dynamic load (Harris et al. 2011). On the other hand, as one of the major characteristics, the bedding structure generally governs the nonlinear mechanical response of bedded shales under dynamic disturbance and plays a critical role in the shale-related projects (Wang et al. 2020c).

Up to now, the split Hopkinson pressure bar (SHPB) system has been used by many researchers (Dai et al. 2016; Shang et al. 2016) to determine the strain-rate dependency of dynamic failure mechanisms which are closely related to the stress wave propagation in heterogeneous rock. Wang et al. (2020b) applied the notched semi-circular bend (NSCB) specimens to investigate the influence of bedding surfaces on the pure mode I and mixed-mode I–II crack propagation of coals. Vervoort et al. (2014) proposed a function between the inclination angle of weak planes and the variation of strengths & final fracture patterns according to the experiment data. Guha Roy and Singh (2016) found that both the heat treatment and layer orientation have strong control on the tensile fracture geometry. Huang et al. (2020) indicated that continental shales are strongly anisotropic in fracture evolution and failure mode. Their experiments also suggested that the uniaxial compressive strength and the degree of fracture exploiting beddings fluctuate in a reverse trend as the bedding angle increases from 0° to 90°. Ma et al. (2018) classified the failure modes of anisotropic rocks into five categories including tensile failure across and along the weakness planes, shear failure across and along the weakness planes, and mixed failure. Fan et al. (2021) found that the shale samples show the obvious phenomenon of post-peak strain softening. Sun et al. (2019) thought that the splitting tensile failure is more likely to occur at a low bedding inclination, and shear or mixed failure is prone to occur at a medium inclination.

In addition to the anisotropic mechanical strength and eventual failure morphology, the fracturing process and failure mode has been another focus for researchers to observe and study (Haeri et al. 2015; 2017; Sarfarazi et al. 2017; Huang et al. 2020). For example, Tien et al. (2006) employed a rotary scanner to obtain the ‘unrolled’ images of rock specimens at different stress levels during the uniaxial compressive tests, facilitating the study of failure processes and failure modes. Ma and Chen (2014) discussed the relationship between meso-damage of shale hydration and soaking time based on the segmentations of CT images. Wu et al. (2016) argued that the meso-scale structure has an important influence on the failure process of samples under various load conditions. Li et al. (2021) proposed a multi-temporal high-accuracy numerical manifold method for transient thermoelastic fracture problems. However, because of the limitation of monitoring means, the mechanical mechanisms

involving the stress buildup, stress shadow and stress transfer (SSS) processes underlying the fracture creation and propagation of bedded shales under dynamic impact remain unclear, and the complex dynamic failure behaviours of heterogeneous rock mass containing mesoscopic pre-existing defects and macroscopic structural planes need to be further investigated.

Besides, the failure of transversely isotropic rock is often more complex than assumed (Dan et al. 2013; Haeri et al. 2014; Duan and Kwok 2015). As a supplement to laboratory tests, the numerical technology has been proven to be a powerful tool to gain a deep understanding of failure mechanisms of anisotropic and inhomogeneous materials (Bahaaddini et al. 2013). Duan et al. (2016) and Liu et al. (2019) modelled the mechanical behaviours of inherently anisotropic rocks in a certain angle range with smooth-joint contacts depending on the discrete element method (DEM). Wang et al. (2018) used the discrete fractures network (DFN) models with different joint distributions to study the directionality of jointed rock mass corresponding to the configurations of laboratory tests. However, for the discrete element model, it is generally difficult to estimate the contact displacements between blocks/particles to guarantee the algorithm convergence and obtain the accurate deformation field (Tang et al. 2000; Brara et al. 2001). Simultaneously, it has obvious difficulties in reproducing fine fracturing process with satisfactory computational efficiency. Zhu and Tang (2006) proposed an elastic damage-based law which can consider the strain-rate dependency to describe the constitutive law based on the rock failure process analysis (RFPA) method (Liang et al. 2015; 2019; Yu et al. 2022). Meng et al. (2021) set up the cohesive zone model to investigate the crack distributions within specimens affected by the number and strength of bedding planes. Wu et al. (2020) concluded that the fractal characteristics of shale become complicated as the osmotic pressure rises by a seepage-stress coupling model. Huang et al. (2020) analyzed the effects of bedding parameters on the length percentage of fractures along the bedding plane and the proportion of tensile and shear cracks. Shang et al. (2018) discussed the effects of bedding lanes with different relative positions and spacings. Xu et al. (2018) suggested that the fracture surface was roughly parallel to the load direction and formed at the centre of the rock disks with loose structure or strong foliation. However, the conventional numerical methods face challenges in dealing with the natural heterogeneity and pre-existing discontinuities of jointed rock mass and modelling the fine dynamic failure process involving the creation, growth and coalescence of cracks under dynamic load conditions.

In this paper, the split Hopkinson pressure bar system was used, and a group of dynamic Brazilian splitting tests were carried out on shale samples. The variation of tensile strengths and failure patterns of samples with different bedding dip angles was therefore studied. Based on the digital image processing (DIP) technology and the RFPA method, the corresponding numerical models were established. The rationality of the numerical approach was verified by the good agreement between the experimental and simulated results. Then, the effects of dip angle and spacing interval of beddings on crack initiation, propagation and coalescence of Brazilian disks under dynamic impact were investigated. Besides, the spatial location and energy magnitude of crack-induced acoustic emissions (AEs) were discussed, and the non-linear

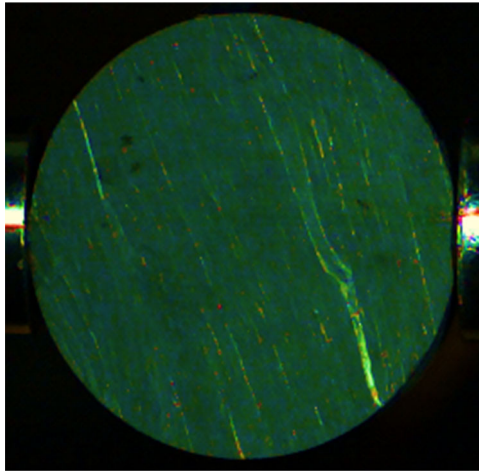


Figure 1. Schematic diagram of the shale sample.

deformation and failure behaviours of bedded shales were further concluded. These achievements will contribute to the stability analysis, supporting design, disaster prevention and mitigation of rock engineering involving bedded shales.

2. Material and method

2.1. Preparation of shale samples

To investigate the anisotropic feature, the shales cored from the outcrops of the formation in Jiangsu Province, China, were selected for this study. The cylindrical samples with the dimensions of 75 mm in diameter and 30 mm in thickness were drilled from the shale strata and prepared for testing according to the recommendation of the International Society for Rock Mechanics (ISRM) (Aminzadeh et al. 2019). **Figure 1** illustrates the schematic diagram of the shale sample. The shale samples consisting of alternate thin weak beddings and thick strong layers generally show the transversely isotropic characteristic, and the beddings/layers are almost parallel to each other.

2.2. Test procedure

The SHPB system has been widely used to determine the dynamic response of rocks. The impact system used in this study was composed of a gas gun, a striker bar, an incident bar, a transmission bar and an absorption bar, as shown in **Figure 2**. The lengths of the striker, incident and transmitted bars were 200 mm, 3000 mm and 1800 mm, respectively. The cylindrical striker and steel bars were made of the hardened 60Si2Mn with the density of 7850 kg/m^3 . The diameter, Young's modulus and P-wave velocity of bars were 38.1 mm, 211 GPa and 5102 m/s, respectively. The pulse shaping technique was used to produce a gentle load rise to effectively achieve dynamic equilibrium in the brittle specimen before its failure. Meanwhile, the copper disc with 3 mm in diameter and 0.6 mm in thickness was used as pulse shaper. The

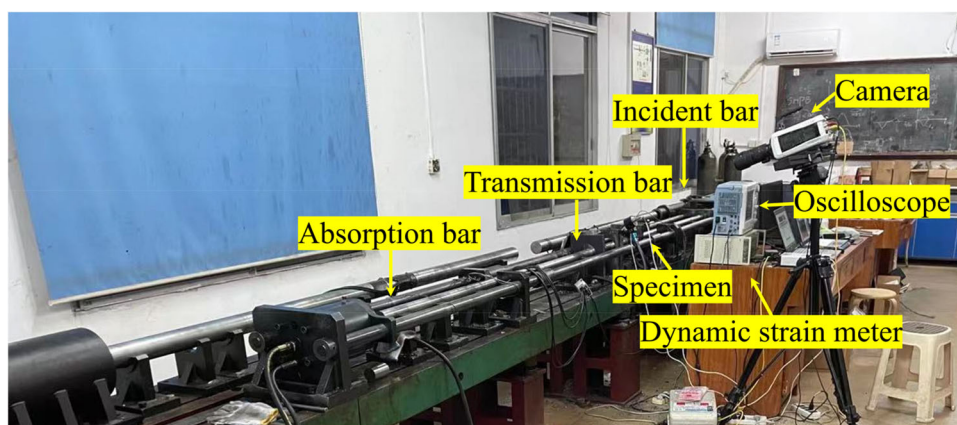


Figure 2. The SHPB system applied in this study.

strain gauges and the dynamic strain amplifier were used to measure the strain of the incident and transmitted bars. An oscilloscope with sampling rate of 10 MHz per second equipped with a computer was used for data analysis and storage. The configuration of the SHPB equipment can be seen in Figure 2. During the impact load, the interval between photos taken by the high-speed camera was 10 μs to record the progressive failure process.

The bars can generate strain when the impact wave propagates in the bars. The incident strain ε_i , reflected strain ε_r and transmitted strain ε_t histories were recorded by the strain gauges mounted on the bars. The three-wave analysis method was used to calculate the displacement and load in a specimen as described below (Lifshitz and Leber 1994; Sharafisafa et al. 2020):

$$P_1(t) = P_2(t) \quad (1)$$

where P_1 and P_2 are the forces acting on the incident end and the transmitted end of the samples, respectively. They can be calculated as follows:

$$P_1(t) = A_0 E [\varepsilon_I(t) + \varepsilon_T(t)] \quad (2)$$

$$P_2(t) = A_0 E \varepsilon_R(t) \quad (3)$$

where ε_I , ε_R and ε_T represent the dynamic strains of the incident, reflected and transmitted waves, respectively; E is the Young's modulus of the bar material; A_0 is the cross-sectional area of the bar.

3 Experimental results and analysis

In the experiments, the velocity of the impact striker was 6 m/s. Figure 3 shows the typical impulse waveforms of the shale disc with a bedding dip angle of 75° in the incident bar and the transmission bar under dynamic impact when the strain rate was 39.10 s^{-1} . According to the ISRM suggested method, the dynamic force

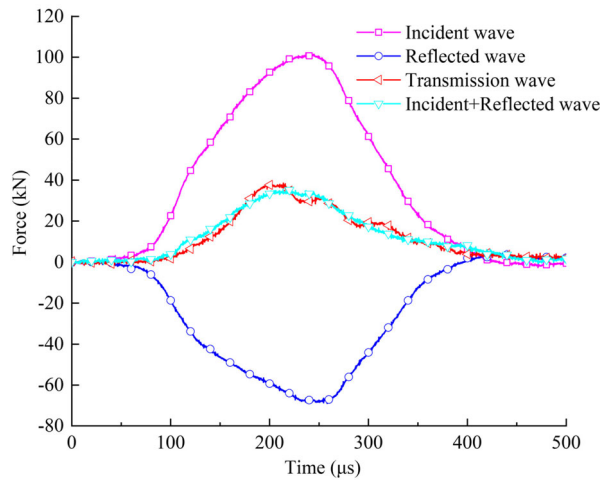


Figure 3. Typical impulse waveforms of the shale disc.

equilibrium should be achieved at both ends of the rock specimen. As shown in [Figure 3](#), a good coincidence between the stress wave curve of ‘Incident wave + Reflected wave’ at the incident end and the stress curve of ‘Transmitted wave’ at the transmitted end indicates that the forces applied on the shale disc were balanced. Therefore, the effectiveness of the dynamic experiment can be guaranteed.

[Figure 4](#) shows the continuous process of the impact failure of the specimens with different bedding dip angles subject to a low strain rate ($\dot{\epsilon} \approx 40 \text{ s}^{-1}$), from which we can see that there are obviously different features regarding crack initiation and propagation, main crack formation and macro fracture occurring in the shale discs with various bedding dip angles. At the first stage, the cracks are generated mainly in the time range of $0 \mu\text{s} \sim 90 \mu\text{s}$. These initial cracks are even invisible due to the very small crack opening. Because of the continuous load, several microcracks are created at the weakest points of the bedding planes. Simultaneously, the tensile strain localization appears at the end of the specimen near the incident bar and extends along the direction of the wave propagation.

With the load time rising to a certain value between $90 \mu\text{s}$ and $190 \mu\text{s}$, the main cracks propagate along different paths influenced by the bedding surfaces. When the bedding angle $\theta = 0^\circ$, the main vertical crack passes through the centre of the specimen and develops basically along the bedding surfaces. At the same time, the local vertical cracks produced near the load jaw form the localized compression zone. When the bedding angle $\theta = 30^\circ$, the main crack shows a more complex circular arc due to the interaction between the vertical load and inclined bedding.

When the bedding angle θ increases to 60° , a primary crack along the load direction and a secondary short crack parallel to the load direction are generated. When the bedding angle θ researches 90° , the vertical main crack develops through the centre line of the specimen and is perpendicular to the bedding plane. Meanwhile, the secondary tensile crack next to the main crack is induced by the tensile stress concentration at the relatively weak bedding plane. As the dynamic impact continues, at the final stage of macroscopic failure, the crack opening becomes larger, and

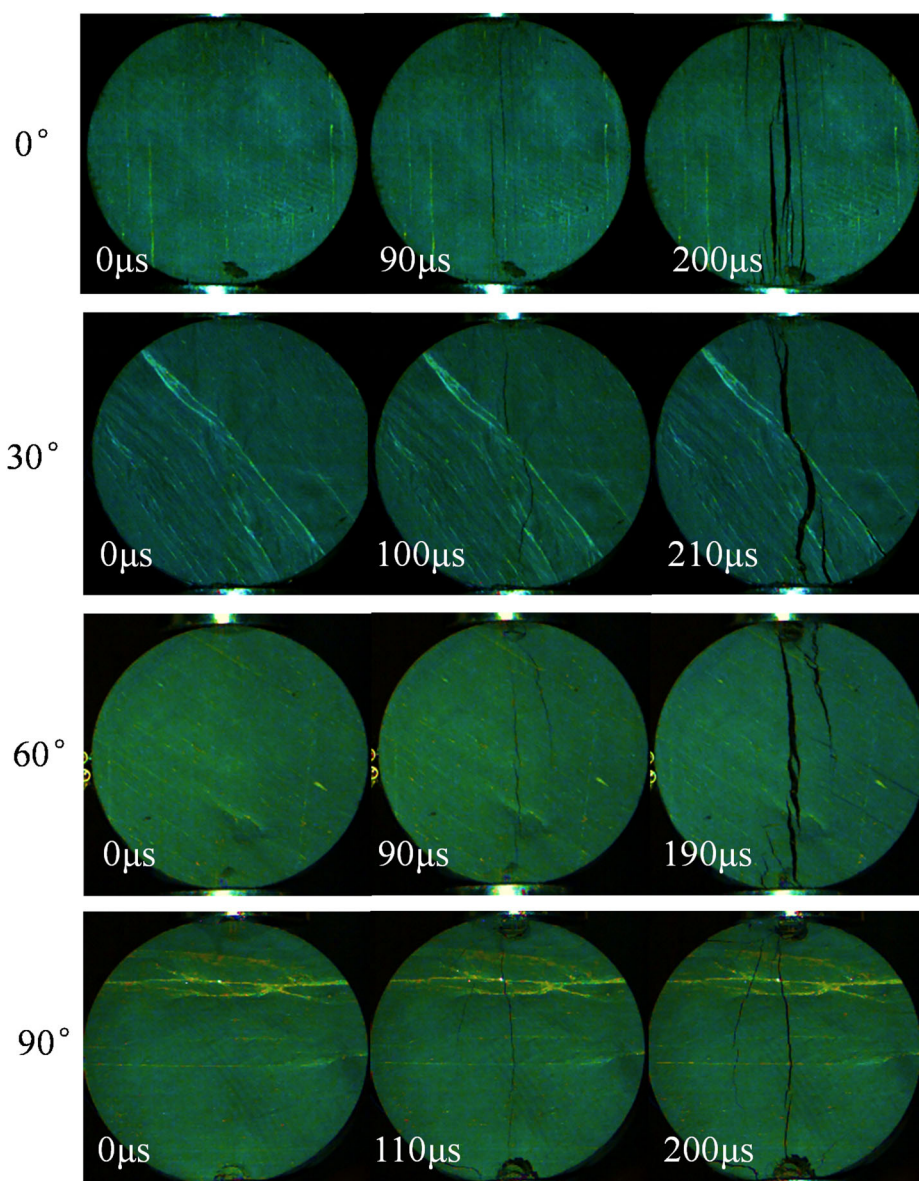


Figure 4. Failure features of the shale discs monitored by the high-speed camera during the dynamic tests.

various fracturing modes can be observed, i.e. along the bedding surface, at the disc centre and along the curved path. Besides, the mechanism can be observed that the cracks are initiated at the weaknesses, the disc continues to produce parallel cracks and cambered cracks induced by the high stresses at the tips of initial cracks, and the macro intersect crack forms due to the gradual coalescence of pre-generated cracks.

The generation and propagation of micro cracks are resulted from both the damage of the bedding planes and the tensile failure initiated at the centre of the disk. Due to the influence of bedding structure, the cracking direction may be changed,

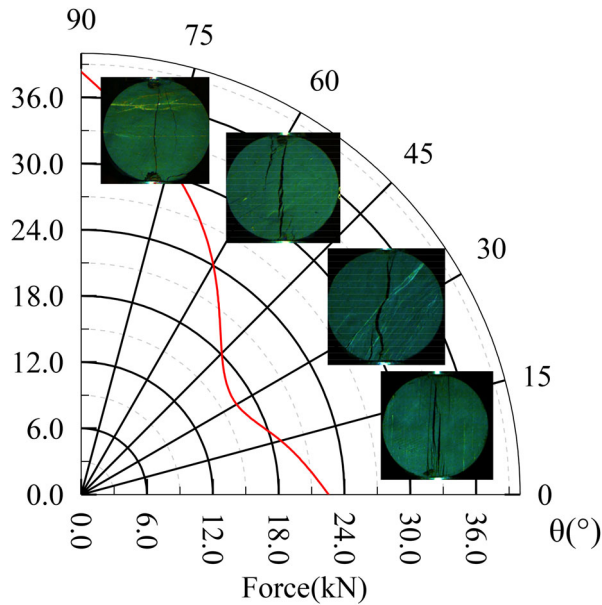


Figure 5. Nominal tensile strength of Brazilian discs with different bedding plane angles.

and the arc-shaped cracks may form. Furthermore, the cracks are able to coalesce and connect between different bedding layers, eventually leading to the macro fracture. Hence, this failure process is significantly affected by the anisotropy and heterogeneity of shale rocks.

Figure 5 shows the variation trend of nominal tensile strengths of shale discs under dynamic Brazilian splitting in the polar coordinates. The strength changes with the bedding angle increasing in the U-shaped trend. Clearly, the tensile strength decreases in the beginning and then increases with the growth of the bedding angle. By comparing the dynamic strength of shales with the quasi-static strength obtained by Khanlari et al. (2015), it can be found that they have great similarity in term of the change trend with the bedding angle rising, i.e. both show the U-shaped changes. After the tensile strength researches the minimum value when the bedding angle θ is around 30° , it increases as the values of θ grows up from 30° to 90° . The maximum tensile strength of shales appears when the bedding angle $\theta = 90^\circ$. Therefore, the strength values are closely related to the inner structural surfaces of shales.

To quantitatively analyze the effect of bedding planes, the statistical crack distributions of the bedding planes and rock matrix were further classified, as shown in Figure 6. Figure 6(a) displays the length variation of the two types of fractures (i.e. in bedding planes and in rock matrix) as a function of the bedding angle θ of shale. It illustrates that the fracture length within rock matrix grows up with the increase of the bedding angle θ . Meanwhile, Figure 6(b) shows that the bedding angle θ has a great influence on the cracking percentage, especially when θ changes from 0° to 30° . Above $\theta = 30^\circ$, the cracking percentages of bedding planes and rock matrix fluctuate. Additionally, the fracture length and cracking percentage of bedding planes show the same changing trend with the bedding angle θ increasing.

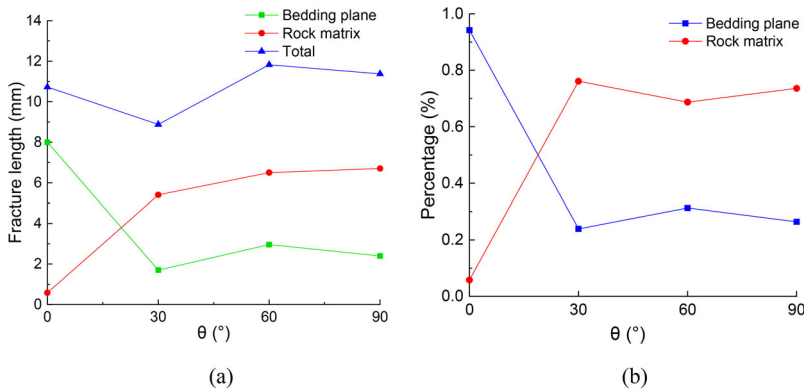


Figure 6. (a) Average fracture length changing with the bedding angle θ and (b) cracking percentage of rock matrix and bedding planes changing with the bedding angle θ .

4 Numerical simulation

4.1. Principal of numerical procedure

To further reveal the mechanical mechanism underlying the failure characteristics of shales, the RFP method (Gong et al. 2019a; 2019b; Chen et al. 2022) and the digital image processing (DIP) (Feng et al. 2022; Gong et al. 2022; Wang et al. 2022a) were combined to capture the stress/strain variation and reproduce the gradual failure process of shale discs numerically. Considering that the shales, as a kind of heterogeneous materials, contain various granular media, holes, micro-cracks and other defects, their mechanical behaviours are closely related to the inner meso-structure, such as stress distribution, crack propagation, damage evolution and failure mode. The DIP-enhanced RFP can effectively characterize the mesoscopic structure of the heterogeneous shales by processing digital image (Wang et al. 2021, 2022b). Clearly, the grey value distribution of the image was analyzed, and the finite element mesh was divided using the pixels. Then, different mesoscopic media were identified according to the thresholds of the grey values. Namely, different material types were determined. The heterogeneity of the same material could be described by a specific statistical function, such as Weibull distribution, normal distribution, *etc.* Among them, the Weibull distribution proposed by Weibull (1951) has been widely used in the field of rock mechanics and rock engineering. The Weibull distribution can be described as follows:

$$f(p) = \frac{m}{p_0} \left(\frac{p}{p_0} \right)^{m-1} \exp - \left(\frac{p}{p_0} \right)^m \quad (4)$$

where p is a specific mechanical parameter of finite elements, such as elastic modulus, cohesion, strength, *etc.*; p_0 is the mean value of the parameter p ; m (>1) reflects the shape of the probability density function, and thus is termed the homogeneity index. For a higher value of m , the rock material will be more uniform, and vice versa. In this study, the mechanical properties of materials were assumed to obey the give Weibull distribution, and the parameter values of the related material elements were

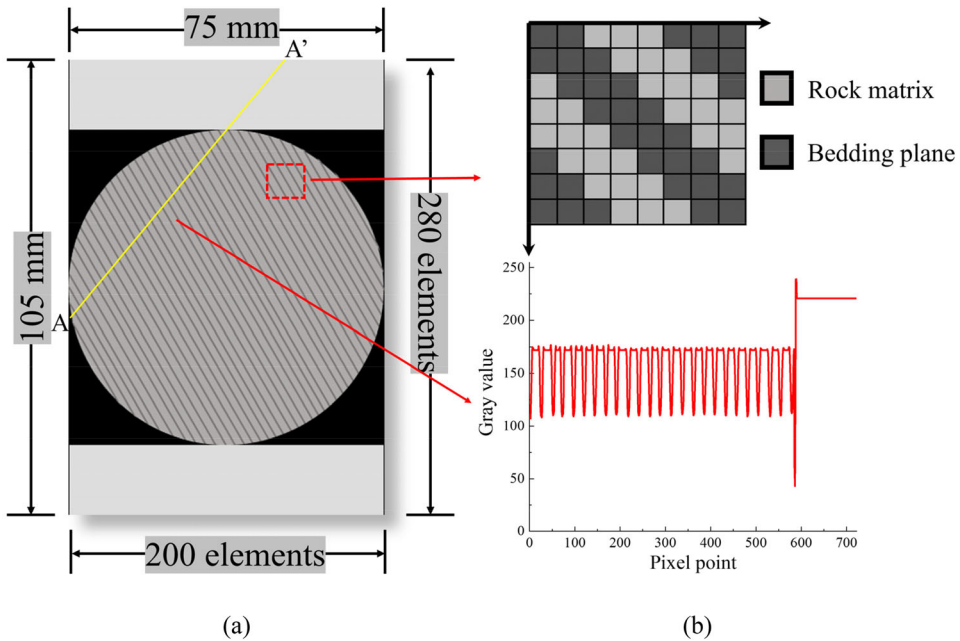


Figure 7. (a) The generated grayscale grid of the digital image and (b) the grey value distribution of different pixels along a specific cross line of the disc.

assigned using the Monte-Carlo method. After that, the numerical model reflecting the mesoscopic structure of the heterogeneous materials was established, as shown in Figure 7(a).

In this study, the purpose of DIP is to identify and characterize the shape and distribution of the bedding layers and the rock matrix using the image threshold segmentation technology. The theoretical principles of the threshold calculation are expressed by Eq. (5). In particular, if the grey value of a pixel is lower than or equal to the threshold T_1 , its grey value will be set to be $1/(n+1)$; if the grey value of the pixel is greater than the threshold T_n , its grey value will be set to 0.

$$f'(x, y) = \begin{cases} 1/(n+1) & f(x, y) \leq T_1 \\ 2/(n+1) & T_1 < f(x, y) \leq T_2 \\ \vdots & \\ n/(n+1) & T_{n-1} < f(x, y) \leq T_n \\ (n+1)/(n+1) & f(x, y) > T_n \end{cases} \quad (5)$$

where $f(x, y)$ is the initial gray value of the pixel (x, y) and $f'(x, y)$ is the gray value of the pixel (x, y) after standardization. The color information of a specific area and the gray curve along a cross line of the disc sample are displayed in Figure 7(b). Additionally, the imported images were segmented according to the three grey thresholds, i.e. T_1 , T_2 and T_3 , as shown in Figure 8, by which the numerical models were established accordingly.

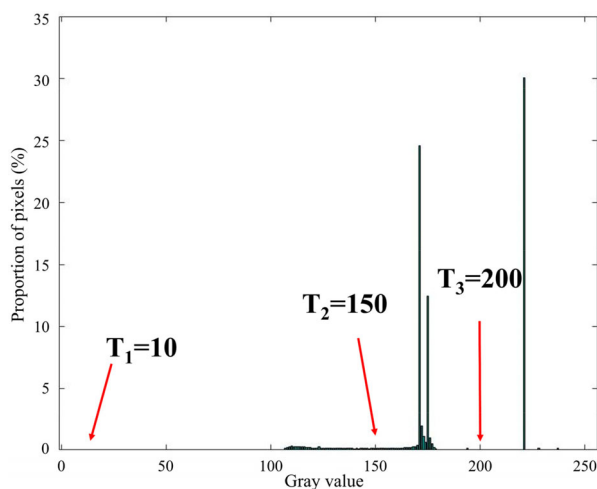


Figure 8. The segmentation thresholds of the imported digital image.

4.2. Model establishment

In this study, the diameter of the numerical discs was 75 mm as shown in [Figure 7](#). The image resolution was 470×660 pixels and the total number of elements composing the model was 310,200. The physical and mechanical parameters used in simulation are listed in [Table 1](#). The bedding dip angle $\theta = 0^\circ, 30^\circ, 60^\circ$ and 90° were taken into account, which was the same as the previous tests. Meanwhile, to understand the effect of bedding spacing on the mechanical response of the shales, three bedding spacing distances were considered, i.e. $S_{bp} = 1.50$ mm, 2.75 mm and 4.00 mm, respectively, while the other parameters remained the same. The incident compressive stress wave simplified from the above physical experiment was applied on the top load plate as shown in [Figure 9](#). The time interval is 0.0001s. The gradual splitting process of the shale discs was simulated based on the plain strain hypothesis. Additionally, the modified Mohr-Coulomb strength criterion with a tensile cut-off was adopted. When an element is subject to the compression-shear stress state, the compression-shear failure will occur if the Mohr-Coulomb strength criterion is satisfied. Meanwhile, when an element is under the tensile stress load, the tensile failure will happen if the maximum tensile strain criterion is triggered.

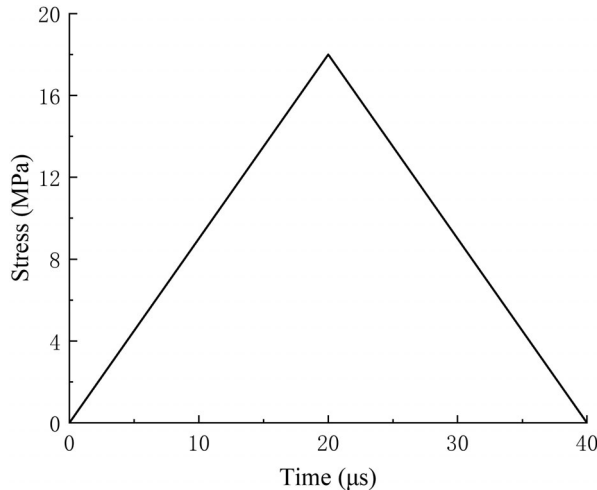
4.3. Numerical results and analysis

4.3.1. Progressive Brazilian splitting

[Figure 10](#) shows the gradual failure process of the sample under dynamic impact, from which it can be seen that the stress wave propagation process in the sample changes along with the damage of the elements in the sample. Before the stress wave propagates to the bottom of the sample, only a few elements located at the top area are damaged. However, cracks initiate near the upper load plate with the load continuing, which is directly caused by the high compression stress. After that, the cracks expand downwards to the lower part of the sample, and multiple obvious cracks occur. Under the further dynamic load, more and more elements at the centre part of

Table 1. Physical and mechanical parameters in simulation.

Parameter	Bedding plane	Matrix	Steel plate
Density (kg/m ³)	2500	2500	7800
Young's modulus (GPa)	5	50	210
Poisson's ratio	0.2	0.2	0.2
Homogeneity index m	3	8	100
Compressive strength (MPa)	50	100	500
Tensile strength (MPa)	5	10	400
Residual strength coefficient	0.1	0.1	1


Figure 9. The incident compressive stress wave applied in simulation.

the sample get damaged and form a tensile fracture zone. Finally, a macro fractured zone composed of multiple cracks is formed along the vertical diameter of the disc. The simulated fracture characteristics and failure mode agree with the experiment well. Hence, the progressive Brazilian splitting was modelled effectively.

4.3.2. Crack propagation of Brazilian discs with different bedding spacings

In this section, the effect of bedding dip angle and bedding spacing on the non-linear deformation and failure behaviours of the Brazilian discs is discussed. Table 2 shows the modelled fracture features and failure patterns by the maximum principal stress contours of the specimens.

When the bedding dip angle $\theta = 0^\circ$, the cracks generate along the vertical bedding surfaces in the middle of the sample, which is consistent with the experimental results as shown in Figure 4. Simultaneously, the sample is separated into the right and left large pieces along the direction parallel to the load axis. However, the bedding spacing shows relatively small effect on the failure mode when $\theta = 0^\circ$. When the bedding dip angle θ increases to 30° and the bedding spacing S_{bp} is 1.50 mm, the main crack forms at the centre of the sample and an inflection point of bending occurs at the middle right part of the sample because of the inclined bedding surfaces, which shows the mixed-mode fracture. This phenomenon also agrees with the above experiment, indicating the reliability and effectiveness of the simulation approach. Furthermore, when the bedding spacing rises to 2.75 mm and 4.00 mm, the single layer activation

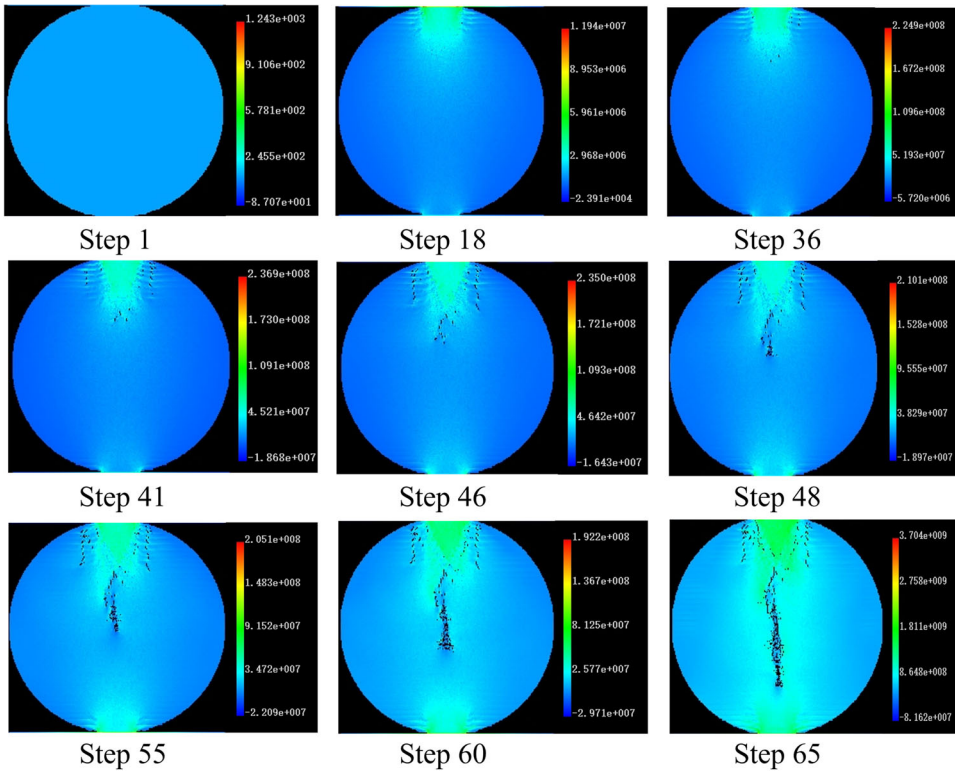
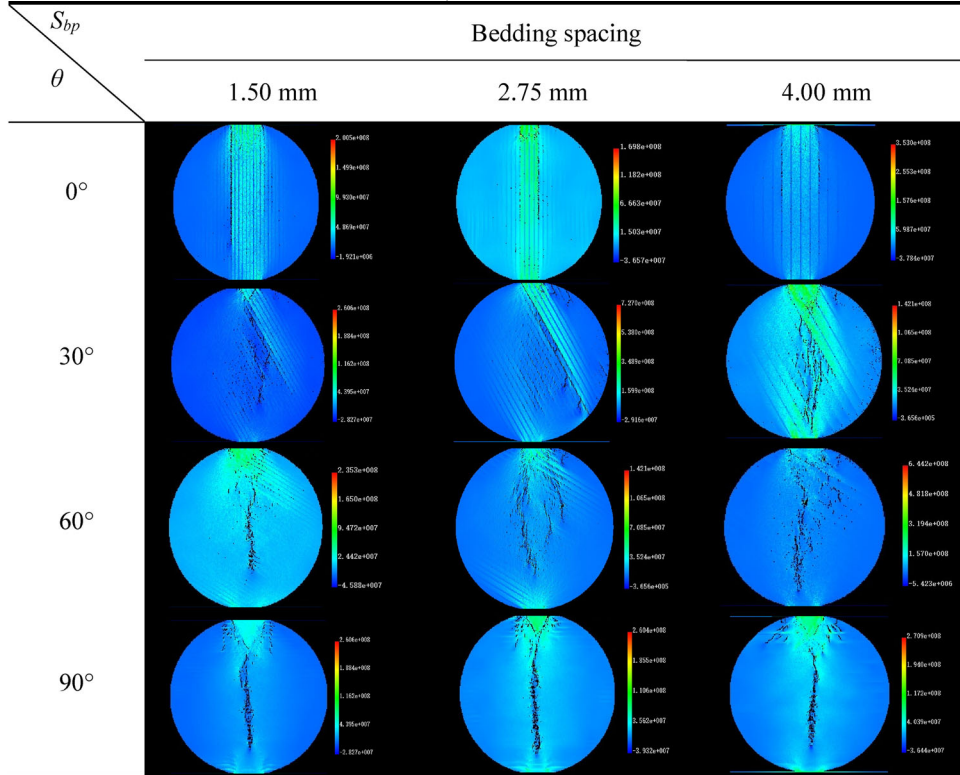


Figure 10. The progressive splitting of the disc by the maximum principal stress contours (unit: Pa).

and central fracture occur for the disk with $\theta = 0^\circ$, respectively. When the bedding dip angle $\theta = 60^\circ$, the main fracture occurs at the centre of the three discs with $S_{bp} = 1.50$ mm, 2.75 mm and 4.00 mm. However, many secondary cracks induced by the high stress concentrations at the inclined bedding surfaces appear at the central fractured zone, which are consistent with the experimental results. When the bedding dip angle $\theta = 90^\circ$, the significant central splitting forms regardless of the change of the bedding spacing distance.

Figure 11(a)–(c) shows the cracking percentage of the bedding planes and the rock matrix changing with three bedding spacings. Generally, the cracking percentage of the bedding surfaces decreases, and the cracking percentage of the rock matrix increases with the bedding dip angle growing up. However, the detailed changing rules are influenced by the bedding spacing. From the Figure 11(d), we can see that for the same dip bedding angle, the cracking percentage changing of the bedding surfaces and the rock matrix are very complicated. When the bedding spacing $S_{bp} = 1.50$ mm, the cracking percentage of the rock matrix rises largely when θ increases from 0° to 30° , and then fluctuates basically at the same level when θ changes from 30° to 90° . Moreover, When the bedding spacing $S_{bp} = 4.00$ mm, the cracking percentage of the rock matrix keeps increasing with a large slope when θ increases from 0° to 60° , and maintains at the same level when θ changes from 60° to 90° . However, when the bedding spacing $S_{bp} = 2.75$ mm, the cracking percentage of the rock matrix

Table 2. The failure patterns of the discs by the maximum principal stress contours (unit: Pa).


keeps rising when θ increases from 0° to 90° . Therefore, the bedding spacing has a great and complex influence on the crack distribution.

The failure force curve of the Brazilian discs of different bedding spacings are all U-shaped changing with the bedding angle increasing, as shown in Figure 12. Namely, the failure force decreases in the beginning and then increases with the bedding angle rising. When the bedding spacing is 1.50 mm, the fracture force at $\theta = 30^\circ$ is the smallest, reaching 45.08 kN. When the bedding spacing is 2.75 mm and 4.00 mm, both the fracture forces at $\theta = 60^\circ$ are the smallest, reaching 51.02 kN and 55.44 kN, respectively. Besides, with the increase of bedding spacing, the fracture forces of the discs with different bedding angles increase in different ways. Clearly, when the bedding spacing is 1.25 mm, the fracture force increases almost linearly at $\theta = 0^\circ$; when the bedding spacing rises from 1.25 mm to 4.00 mm, the fracture force increases from 45.02 kN to 57.67 kN with a ratio of about 28% at $\theta = 30^\circ$; when $\theta = 60^\circ$ and 90° , this increment of fracture force is about 5.44 kN and 4.94 kN, respectively. Hence, the fracture force is significantly affected by the interaction of bedding spacing and bedding angle.

4.3.3. Acoustic emission analysis

When the rock-like quasi-brittle material get damaged, the elastic wave may be released in the form of AE. The generation of transient elastic wave reflects the rapid

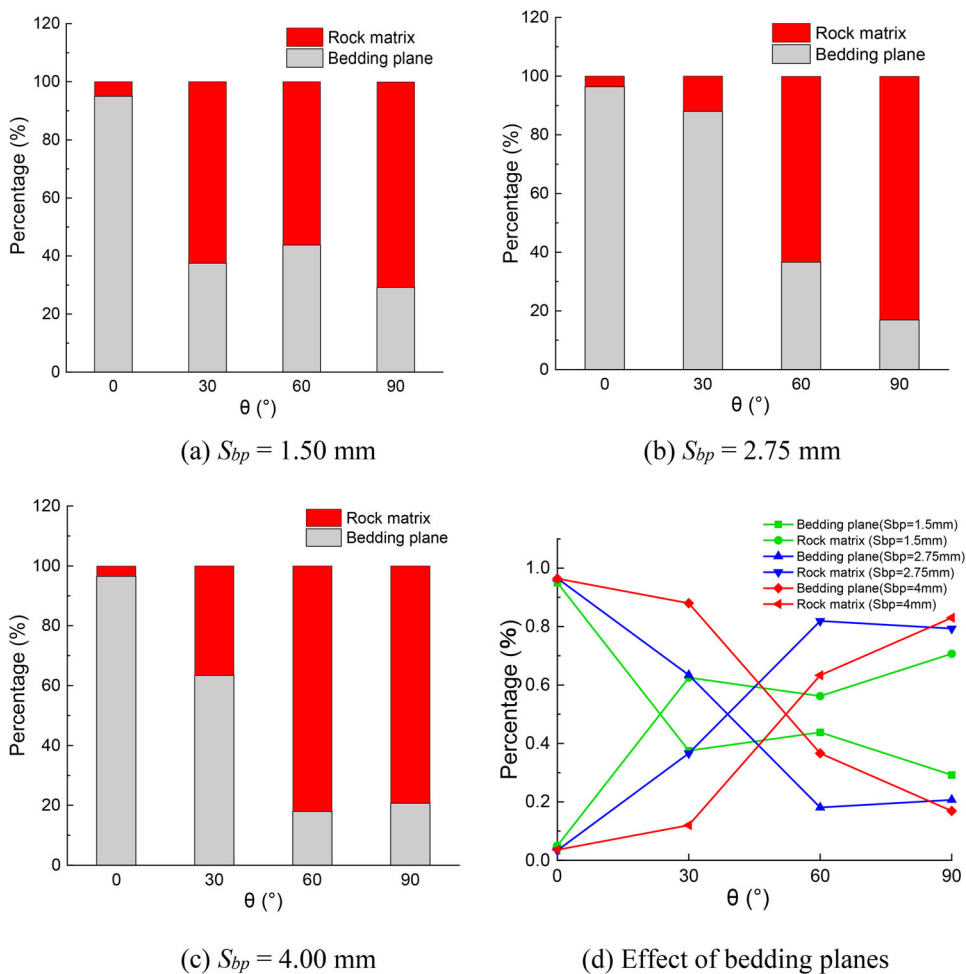


Figure 11. Cracking percentage of rock matrix and bedding planes.

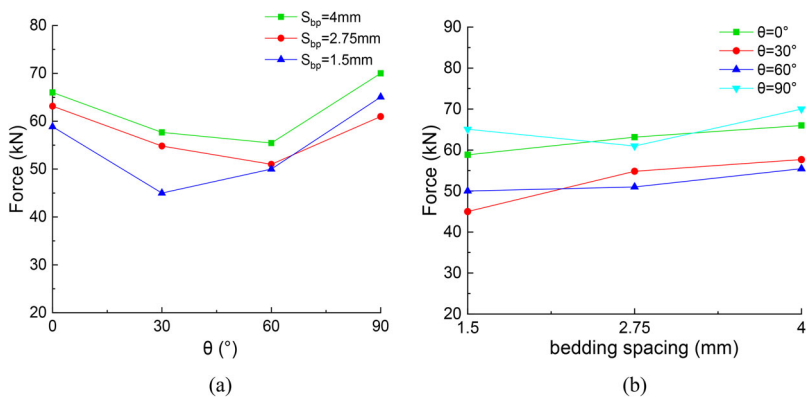


Figure 12. Effect of bedding dip angle and bedding spacing on fracture force.

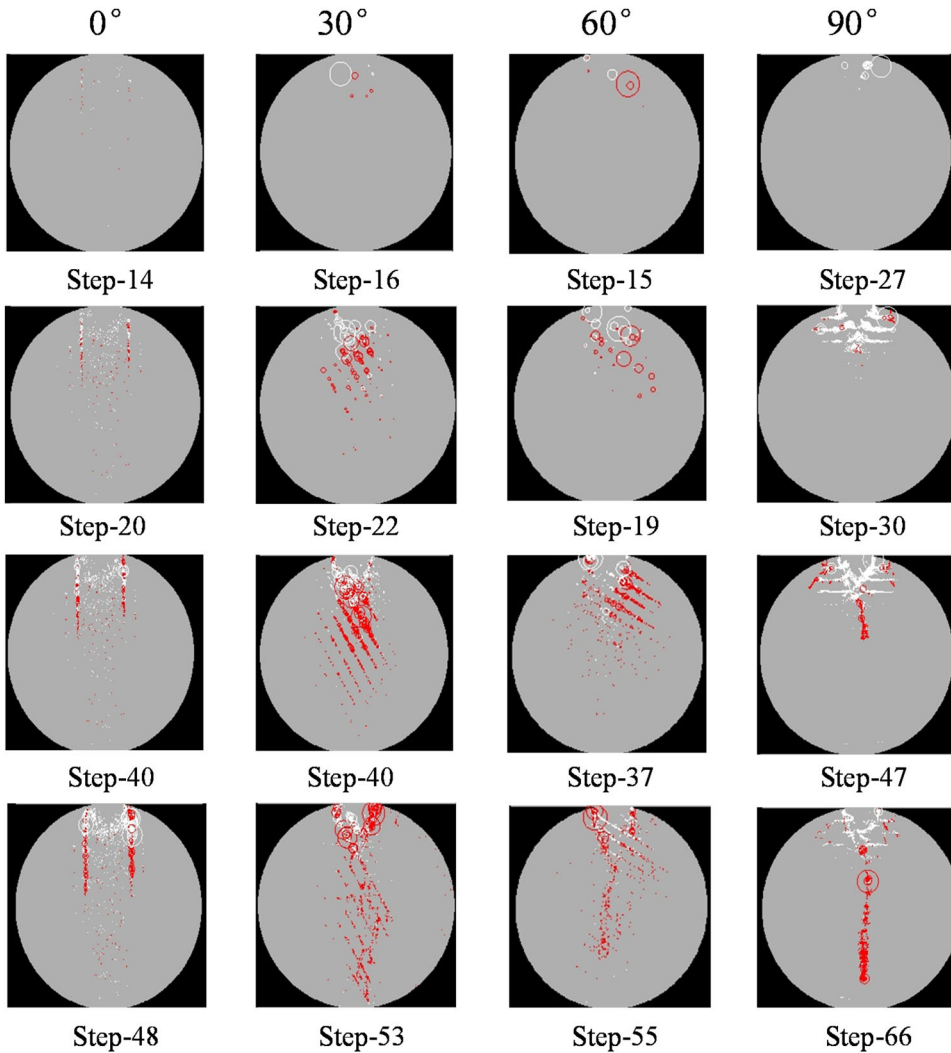


Figure 13. AE distribution of the shale discs when the bedding spacing $S_{bp} = 4.00$ mm.

energy release in a local region. Therefore, to investigate the spatiotemporal evolution rules of elastic energy of the shales induced by crack initiation and growth under dynamic impact, the spatial distribution and magnitude of the AE events will be discussed in this section. Figures 13–18 shows the simulated AE performance during the failure process of the shale discs. They illustrate that each AE reflects the failure of an element in the shale model, and the number of AEs is directly proportional to the number of damaged elements. Note that the red circle represents an AE event occurring due to the tensile failure of an element, while the white circle represents an AE event occurring due to the compression-shear failure of an element. The radius of a circle is proportional to the magnitude of released energy.

The first row of Figure 13 shows a few elements are damaged because of the compression-shear strength criterion is satisfied, and several AE events release relatively large energy near the incident plate at the initial stage of dynamic load. With the

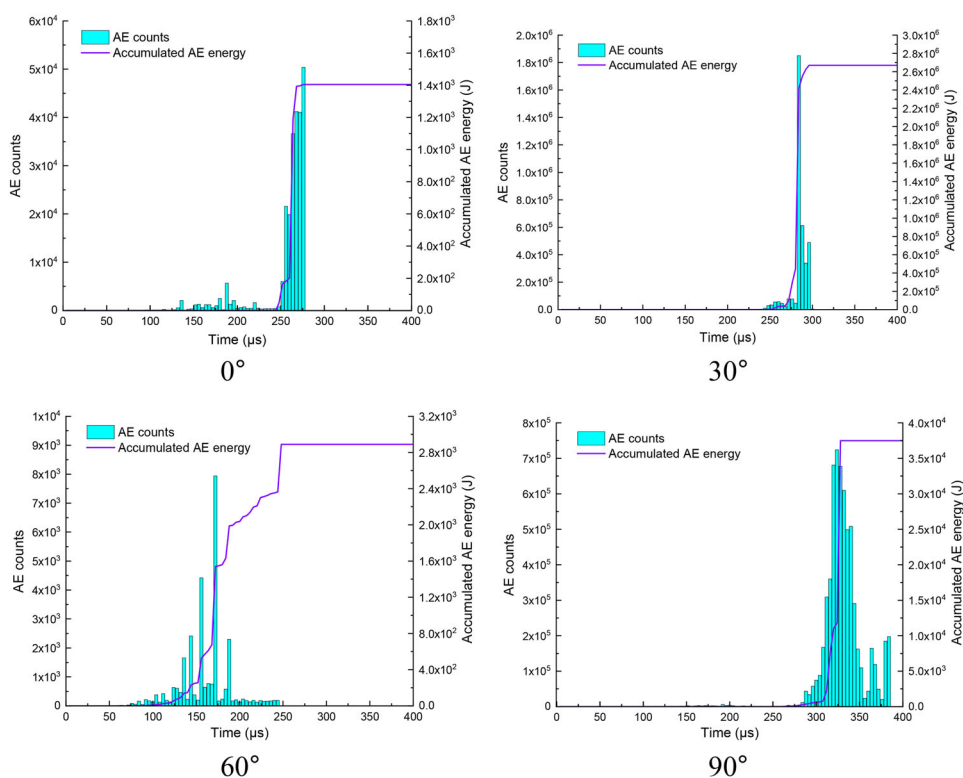


Figure 14. AE events and energy at different failure stages when the bedding spacing $S_{bp} = 4.00$ mm.

load stress increasing, some micro-cracks are created at the weakest parts of the shale disc, as shown in the second row of Figure 13. In particular, when the bedding angle $\theta = 90^\circ$, the compression failures happen obviously along the bedding planes at the top area of the sample, forming a group of parallel rupture bands. As the dynamic stress wave continues to propagate downward, the strength thresholds of more and more meso-elements are researched, and the previous cracks further propagate and evolves basically along the vertical or inclined bedding planes when the bedding angle $\theta = 0^\circ$, 30° and 90° . However, for $\theta = 90^\circ$, a vertical broken zone across the bedding surfaces is induced by the high tensile stress below the previously formed horizontal compression bands. The fourth row of Figure 13 shows the spatial positions of all the AE events when the final failure modes form, from which we can see that the tensile damage plays a critical role in leading to the macro failure of bedded shales under splitting.

Furthermore, Figure 14 shows the corresponding AE counts and accumulated AE energy during the Brazilian splitting. At the initial stage of dynamic load, the number of AE events increases a bit, and the cumulative energy curves rise slowly, showing an overall upward trend. During the evolution and development of cracks, the AE counts begin to grow up. At the beginning of macro failure, the AE count curves start to increase rapidly with a sharp slope, demonstrating that the samples begin to generate many AE signals. Simultaneously, the cumulative energy reaches the maximum

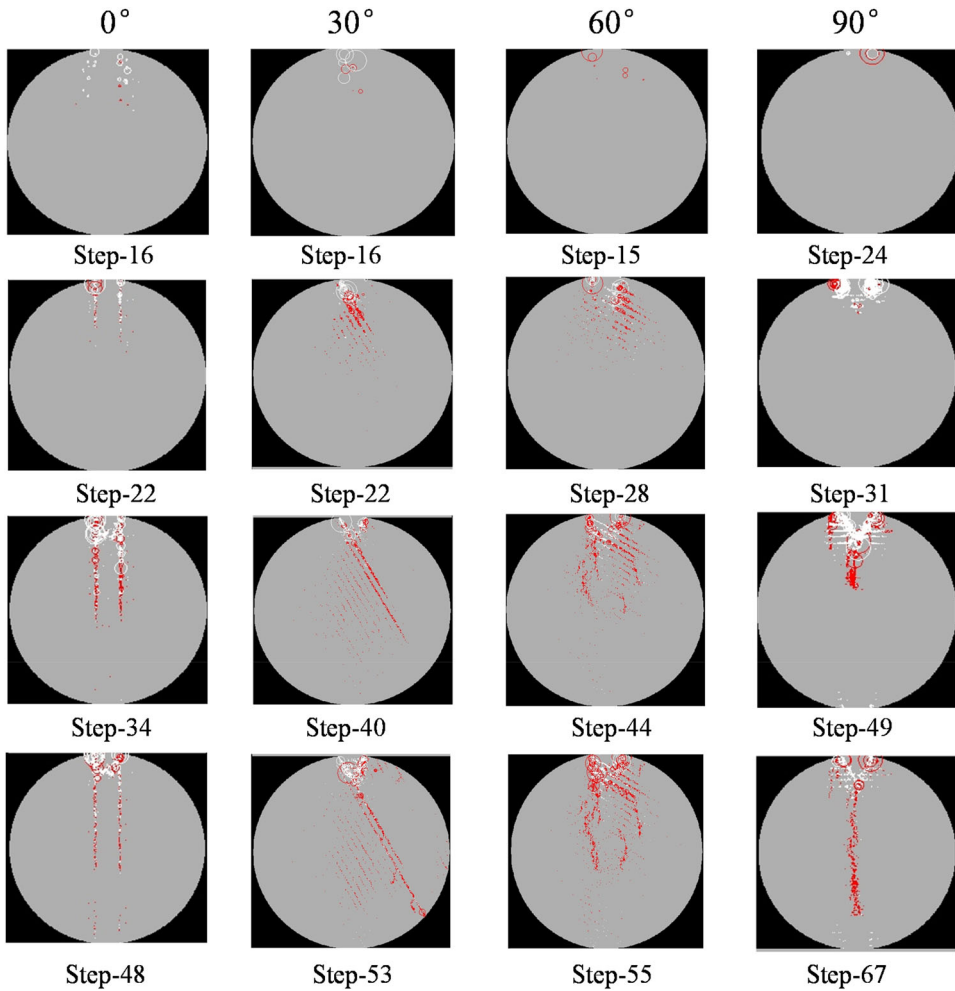


Figure 15. AE distribution of the shale discs when the bedding spacing $S_{bp} = 2.75$ mm.

value very quickly. Therefore, the acceleration of the cracking growth and the rapid growth of AE energy can be regarded as the reliable precursors of shale failure. With the coalescence and connection of the previously formed cracks, the macro main fracture gradually occurs, and the cumulative AE energy reaches its peak value. After that, although the AE activities are weakened, the AE events are still active, indicating that the specimens have residual strength, and there are elements still getting damaged.

Figure 15 shows the AE spatial evolution characteristics of the shale discs with different bedding dip angles when the bedding spacing becomes dense to 2.75 mm. The first row illustrates that at the beginning of dynamic load, several AE events are caused by the damage of the rock near the incident plate. Especially, when the bedding angle $\theta = 0^\circ$, the compression-shear damages are the majority. As the load stress increases, when the bedding angle $\theta = 0^\circ$, 30° and 60° , the cracks develop downwards, but the propagation paths are greatly affected by the existence of the bedding surfaces. However, for $\theta = 90^\circ$, two small compression rupture zones form beneath the

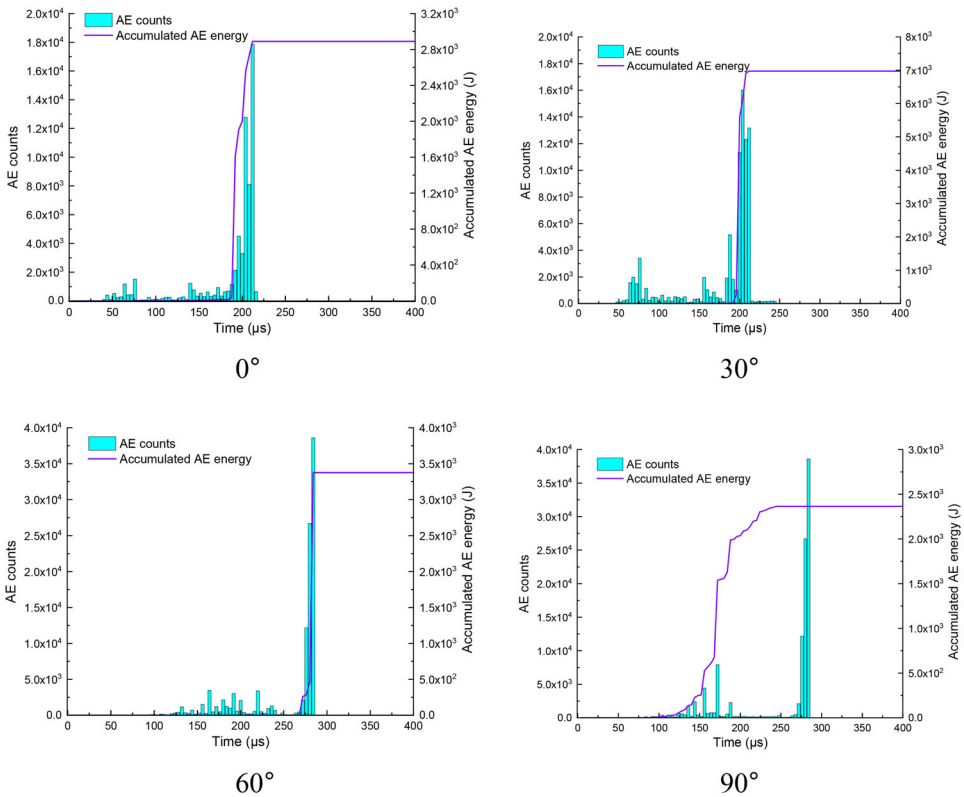


Figure 16. AE events and energy at different failure stages when the bedding spacing $S_{bp} = 2.75$ mm.

two ends of the upper load plate. With the dynamic stress wave propagating, the development direction of cracks is along the bedding surfaces when $\theta = 0^\circ$ and 30° . But when θ increases to 60° , the rock between adjacent beddings at the middle upper part of the disc are more seriously damaged due to the large inclination. Simultaneously, an obvious triangle compression rupture zone occurs beneath the upper load plate. The fourth row of Figure 15 illustrates that the elements are mainly damaged in the tensile mode because of the high tensile stress concentrations at the centre of the disc.

Figure 16 shows the AE counts and accumulated AE energy when the bedding spacing $S_{bp} = 2.75$ mm, from which it can be seen that at the beginning of Brazilian splitting, the AE events appear sporadically, and there is no large energy released through AEs. With more and more cracks being initiated and developing, the number of AE events gradually increase, but the cumulative AE energy is still relatively small. As the macro failure is coming, the AE counts and cumulative AE energy curves begin to increase rapidly with a sharp slope, which can be treated as the precursor of shale instability. Particularly, for $\theta = 90^\circ$, more AE events were generated after macro failure, but the released energy is small, indicating that the sample still has a certain residual strength.

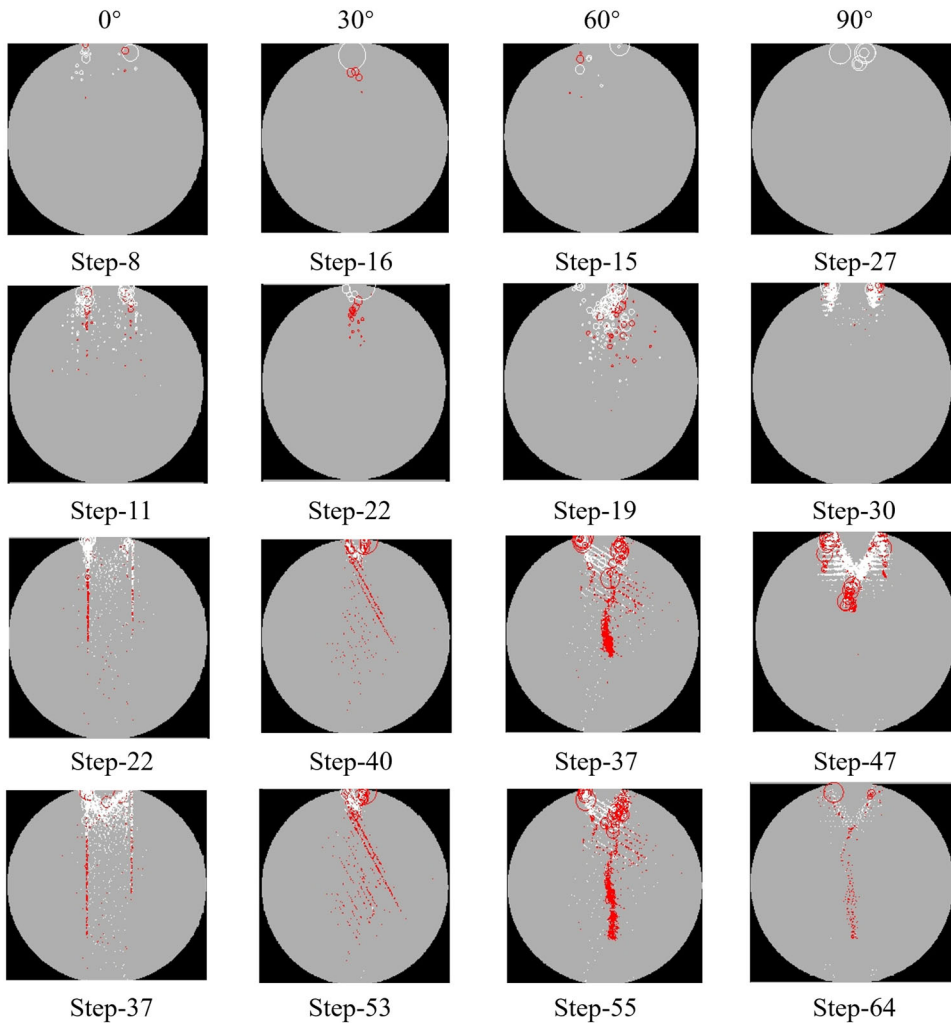


Figure 17. AE distribution of the shale discs when the bedding spacing $S_{bp} = 1.50$ mm.

Figure 17 displays the AE spatial evolution of the samples with different bedding dip angles when the bedding spacing is 1.50 mm, meaning that the bedding surfaces are denser. The first row shows that at the initial stage of dynamic impact, several AE events distribute near the incident plate, which are the same as the previous two situations when $S_{bp} = 4.00$ mm and 2.75 mm. Meanwhile, the compression-shear damages are the majority. With the load stress rising, more and more AE events are caused at the middle upper part of the samples. But their distribution is scattered for $\theta = 0^\circ$, 30° and 60° . For $\theta = 90^\circ$, two serious damaged areas occur under the incident plate. As the dynamic stress wave keeps propagating, the cracks develop downwards straightly when $\theta = 0^\circ$. However, the propagation paths are changed by the oblique bedding surfaces when θ grows up to 30° and 60° . Particularly, for $\theta = 60^\circ$, a bending crack forms because of the damage of the rock between adjacent beddings at the centre of the disc. Simultaneously, a triangle compression fractured zone is caused by

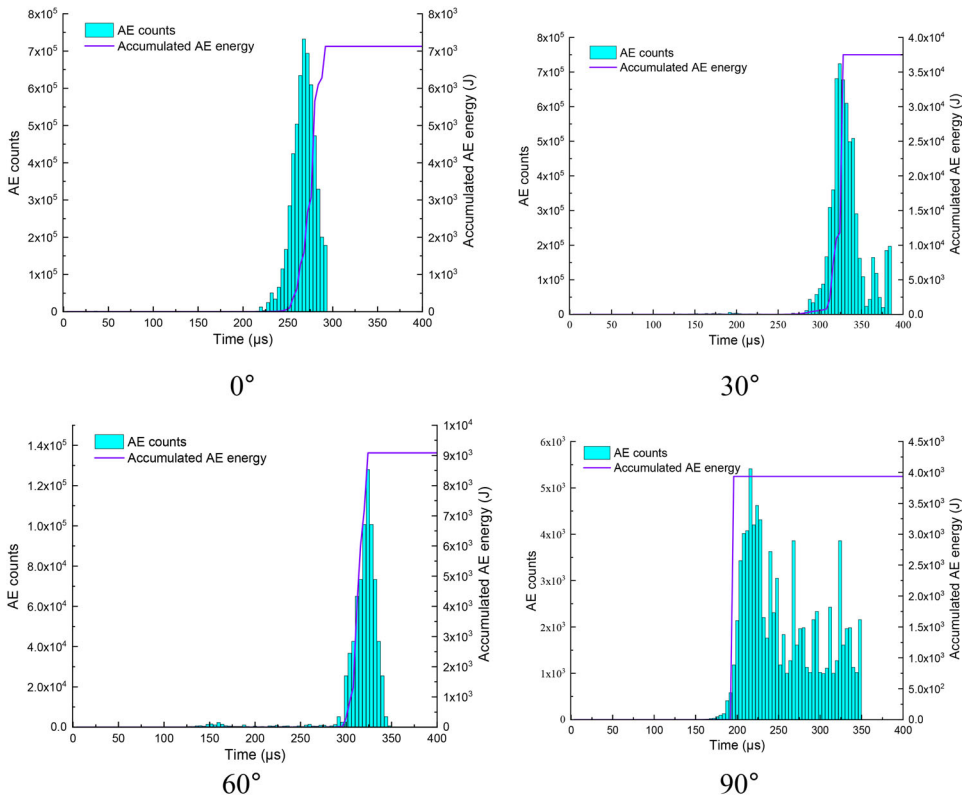


Figure 18. AE events and energy at different failure stages when the bedding spacing $S_{bp} = 1.50$ mm.

the high compressive stress in this area. The fourth row of Figure 17 illustrates that when the bedding angle $\theta = 0^\circ$, two vertical tensile cracks occur, between which many elements are damaged in the compression-shear mode; when $\theta = 30^\circ$, the tensile cracks are mainly along the inclined beddings; when $\theta = 60^\circ$ and 90° , the centre of the disc is damaged seriously due to the high tensile stress concentrations except the triangle compressive fractured zone at the top.

In addition, Figure 18 displays the corresponding AE counts and accumulated AE energy during the Brazilian splitting when the bedding spacing $S_{bp} = 1.50$ mm. It shows that at the initial stage of dynamic load, only a small number of AE events are caused, and the cumulative released energy is very low. But the overall trend is upward. With the initiation and evolution of more cracks, the AE counts and the cumulative AE energy start to grow up little by little. Especially, at the beginning of macro failure of the samples, they keep rising rapidly with a sharp slope. Hence, the quick growth of cumulative AE energy can be recognized as the effective precursor of shale failure. However, note that when the bedding dip angle $\theta = 30^\circ$ or 60° , the AE counts and the AE energy reach their peak values basically at the same time. But for $\theta = 0^\circ$, the maximum AE energy lags behind the maximum AE counts, indicating that many non-penetrating cracks are created before macro failure. Besides, when the

bedding dip angle $\theta = 90^\circ$, a lot of AE events continue to be generated after macro failure, indicating that the sample still has a relatively high residual strength.

5. Conclusions

In this study, to reveal the influence of bedding surfaces on the anisotropic deformation and strength characteristics of shales under dynamic impact, a series of Brazilian disc tests were conducted by the SHPB system. Meanwhile, the fracturing process and failure modes were monitored by the high-speed camera. Furthermore, to understand the fracture creation and propagation mechanism, the stress buildup, stress shadow and stress transfer were modelled based on the DIP technology and the RFPA method. The conclusions can be summarized as follows:

1. At the beginning of dynamic load, several microcracks initiate at the weakest points of the bedding planes and these initial cracks are even invisible due to very small crack opening. Then, because of the effect of bedding structure, the cracking direction may be changed, and the arc-shaped cracks may form. Furthermore, the cracks can coalesce and penetrate between adjacent bedding layers, eventually leading to the macro fracture. Namely, the shale discs gradually produce parallel and cambered cracks induced by the high stresses at the tips of initial cracks, and the macro intersect cracks form due to the progressive development and coalescence of pre-generated cracks.
2. The tensile strength of shale discs under dynamic Brazilian splitting changes in the U-shaped trend with the bedding angle increasing because the macroscopic fracture mode varies. Simultaneously, with the growth of the bedding angle θ , the total fracture length within rock matrix grows up. Furthermore, the bedding angle θ has a strong influence on the cracking percentage, especially when θ changes from 0° to 30° . Above $\theta=30^\circ$, the cracking percentages of bedding planes and rock matrix display a fluctuating trend. Additionally, the fracture length and cracking percentage of bedding planes show the same changing trend with the bedding angle θ increasing.
3. There is a good agreement between the numerical simulation and the SHPB experiment in terms of fracture characteristics and failure modes. When the bedding dip angle θ is 30° and the bedding spacing S_{bp} is 1.50 mm, the main crack forms at the centre of the sample and an inflection point of bending occurs at the middle right part of the sample because of the inclined bedding surfaces, which shows the mixed-mode fracture. Meanwhile, when the bedding dip angle θ is 60° , the main fracture occurs at the centre of the three discs with $S_{bp} = 1.50$ mm, 2.75 mm and 4.00 mm. However, many secondary cracks induced by the high-stress concentrations at the inclined bedding surfaces appear at the central fractured zone. Besides, when the bedding dip angle $\theta = 90^\circ$, the significant central splitting forms regardless of the change of bedding spacing distance.
4. Basically, the cracking percentage of the bedding surfaces decreases, but the cracking percentage of the rock matrix increases with the bedding dip angle growing up. Meanwhile, the failure force curves of the Brazilian discs with

different bedding spacings are all U-shaped changing with the bedding angle increasing. Additionally, at the beginning of macro failure, the AE counts start to increase rapidly with a sharp slope, demonstrating that the samples begin to generate many AE signals. Simultaneously, the cumulative energy reaches the maximum value very quickly. Therefore, the acceleration of the cracking growth and the rapid growth of AE energy can be regarded as the effective precursors of shale failure.

Disclosure statement

The authors declare that they have no known competing financial interests or personal relationships that could appear to influence the work reported here.

Data availability

The datasets generated and/or analyzed during the current study are available from the corresponding author upon reasonable request.

Funding

This work was supported by the National Natural Science Foundation of China (Grant Nos. 41941018, 42102314 and 42050201) and the China Postdoctoral Science Foundation (Grant No. 2020M680950). The authors are grateful for these supports.

ORCID

Xianhui Feng  <http://orcid.org/0000-0002-2379-1103>

Bin Gong  <http://orcid.org/0000-0002-9464-3423>

References

- Aminzadeh A, Fahimifar A, Nejati M. 2019. On Brazilian disk test for mixed-mode I/II fracture toughness experiments of anisotropic rocks. *Theor Appl Fracture Mech.* 102:222–238.
- Bahaaddini M, Sharrock G, Hebblewhite BK. 2013. Numerical investigation of the effect of joint geometrical parameters on the mechanical properties of a non-persistent jointed rock mass under uniaxial compression. *Comput Geotech.* 49:206–225.
- Brara A, Camborde F, Klepaczko JR, Mariotti C. 2001. Experimental and numerical study of concrete at high strain rates in tension. *Mech Mater.* 33(1):33–45.
- Chen BP, Gong B, Wang SY, Tang, C, A. 2022. Research on zonal disintegration characteristics and failure mechanisms of deep tunnel in jointed rock mass with strength reduction method. *Mathematics.* 10(6):922.
- Dai F, Xu Y, Zhao T, Xu N-w, Liu Y. 2016. Loading-rate-dependent progressive fracturing of cracked chevron-notched Brazilian disc specimens in split Hopkinson pressure bar tests. *Int J Rock Mech Mining Sci.* 88:49–60. <https://doi.org/10.1016/j.ijrmms.2016.07.003>.
- Dan DQ, Konietzky H, Herbst M. 2013. Brazilian tensile strength tests on some anisotropic rocks. *Int J Rock Mech Mining Sci.* 58:1–7.
- Duan K, Kwok CY, Pierce M. 2016. Discrete element method modeling of inherently anisotropic rocks under uniaxial compression loading. *Int J Numer Anal Meth Geomech.* 40(8): 1150–1183.

- Duan K, Kwok CY. 2015. Discrete element modeling of anisotropic rock under Brazilian test conditions. *Int J Rock Mech Mining Sci.* 78:46–56.
- Eliyahu M, Emmanuel S, Day-Stirrat RJ, Macaulay CI. 2015. Mechanical properties of organic matter in shales mapped at the nanometer scale. *Marine Petrol Geol.* 59:294–304.
- Fan X, Luo N, Liang H, Sun X, Zhai C, Xie L. 2021. Dynamic breakage characteristics of shale with different bedding angles under the different ambient temperatures. *Rock Mech Rock Eng.* 54(6):3245–3261.
- Feng XH, Gong B, Tang CA, Zhao T. 2022. Study on the non-linear deformation and failure characteristics of EPS concrete based on CT-scanned structure modelling and cloud computing. *Eng Fract Mech.* 261:108214.
- Gong B, Tang CA, Wang SY, Bai H, M, Li YC. 2019a. Simulation of the nonlinear mechanical behaviors of jointed rock masses based on the improved discontinuous deformation and displacement method. *Int J Rock Mech Mining Sci.* 122:104076.
- Gong B, Wang SY, Sloan SW, Shen DC, Tang CA. 2019b. Modelling rock failure with a novel continuous to discontinuous method. *Rock Mech Rock Eng.* 52(9):3183–3195.
- Gong B, Wang YY, Zhao T, Tang CA, Yang XY, Chen, T, T. 2022. AE energy evolution during CJB fracture affected by rock heterogeneity and column irregularity under lateral pressure. *Geomatic Nat Hazard Risk.* 13(1):877–907.
- Guha Roy D, Singh TN. 2016. Effect of heat treatment and layer orientation on the tensile strength of a crystalline rock under Brazilian test condition. *Rock Mech Rock Eng.* 49(5): 1663–1677. <https://doi.org/10.1007/s00603-015-0891-y>.
- Haeri H, Khaloo A, Marji MF. 2015. Experimental and numerical simulation of the microcrack coalescence mechanism in rock-like materials. *Strength Mater.* 47(5):740–754.
- Haeri H, Sarfarazi V, Yazdani M, Shemirani AB, Hedayat A. 2018. Experimental and numerical investigation of the centre-cracked horseshoe disc method for determining the mode I fracture toughness of rock-like material. *Rock Mech Rock Eng.* 51(1):173–185.
- Haeri H, Sarfarazi V, Zhu Z. 2017. Effect of normal load on the crack propagation from pre-existing joints using Particle Flow Code (PFC). *Comput Concrete.* 19(1):99–110.
- Haeri H, Shahriar K, Marji MF, Moarefvand P. 2014. Investigation of fracturing process of rock-like brazilian disks containing three parallel cracks under compressive line loading. *Strength Mater.* 46(3):404–416.
- Harris NB, Miskimins JL, Mnich CA. 2011. Mechanical anisotropy in the Woodford Shale, Permian Basin: origin, magnitude, and scale. *Leading Edge.* 30(3):284–291. <https://doi.org/10.1190/1.3567259>.
- Huang B, Li L, Tan Y, Hu R, Li X. 2020. Investigating the meso-mechanical anisotropy and fracture surface roughness of continental shale. *JGR Solid Earth.* 125(8):e2019JB017828.
- Huang D, Li B, Ma WZ, Cen DF, Song YX. 2020. Effects of bedding planes on fracture behavior of sandstone under semicircular bending test. *Theor Appl Fracture Mech.* 108:102625.
- Khanlari GR, Heidari M, Sepahigero AA, Fereidooni D. 2014. Quantification of strength anisotropy of metamorphic rocks of the Hamedan province, Iran, as determined from cylindrical punch, point load and Brazilian tests. *Eng Geol.* 169:80–90.
- Khanlari G, Rafiei B, Abdilor Y. 2015. An Experimental investigation of the Brazilian tensile strength and failure patterns of laminated sandstones. *Rock Mech Rock Eng.* 48(2):843–852.
- Li A, Liu Y, Dai F, Liu K, Wei M. 2020. Continuum analysis of the structurally controlled displacements for large-scale underground caverns in bedded rock masses. *Tunnelling Underground Space Technol.* 97:103288.
- Li G, Wang K, Gong B, Tao Z, Du K, Tang C. 2021. A multi-temporal series high-accuracy numerical manifold method for transient thermoelastic fracture problems. *Int J Solid Struct.* 230-231:111151.
- Liang ZZ, Gong B, Wu XK, Zhang YB, Tang CA. 2015. Influence of principal stresses on failure behavior of underground openings. *Chin J Rock Mech Eng.* 34(s1):3176–3187.
- Liang ZZ, Gong B, Li W. 2019. Instability analysis of a deep tunnel under triaxial loads using a three-dimensional numerical method with strength reduction method. *Tunnelling Underground Space Technol.* 86:51–62.

- Lifshitz JM, Leber H. 1994. Data processing in the split Hopkinson pressure bar tests. *Int J Impact Eng.* 15(6):723–733.
- Liu ZJ, Zhang CQ, Zhang CS, Gao Y, Zhou H, Chang, Z, R. 2019. Deformation and failure characteristics and fracture evolution of cryptocrystalline basalt. *J Rock Mech Geotech Eng.* 11(5):990–1003.
- Ma L, Wang M, Zhang N, Fan P, Li JA. 2017. Variable-parameter creep damage model incorporating the effects of loading frequency for rock salt and its application in a bedded storage cavern. *Rock Mech Rock Eng.* 50(9):2495–2509.
- Ma T, Chen P. 2014. Study of meso-damage characteristics of shale hydration based on CT scanning technology. *Petrol Explorat Develop.* 41(2):249–256.
- Ma T, Peng N, Zhu Z, Zhang Q, Yang C, Zhao J. 2018. Brazilian tensile strength of anisotropic rocks: review and new insights. *Energies.* 11(2):304.
- Meng Y, Jing H, Liu X, Yin Q, Wei X. 2021. Experimental and numerical investigation on the effects of bedding plane properties on the mechanical and acoustic emission characteristics of sandy mudstone. *Eng Fract Mech.* 245:107582.
- Sarfarazi V, Haeri H, Shemirani AB, Zhu Z. 2017. Shear behavior of non-persistent joint under high normal load. *Strength Mater.* 49(2):320–334.
- Shang J, Duan K, Gui Y, Handley K, Zhao Z. 2018. Numerical investigation of the direct tensile behaviour of laminated and transversely isotropic rocks containing incipient bedding planes with different strengths. *Comput Geotech.* 104:373–388.
- Shang J, Hencher S, R, West, L, J. 2016. Tensile strength of geological discontinuities including incipient bedding, rock joints and mineral veins. *Rock Mech Rock Eng.* 49(11):4213–4225.
- Sharafisafa M, Aliabadian Z, Shen L. 2020. Crack initiation and failure development in bim-rocks using digital image correlation under dynamic load. *Theor Appl Fracture Mech.* 109: 102688.
- Sun Q, Zhang Z, Peichao LI, Sun Z, Detang LU, Gao F. 2019. Study on the bedding effect and damage constitutive model of black shale under dynamic loading. *Chin J Rock Mech Eng.* 38:1319–1331.
- Suo Y, Chen Z, Rahman SS, Song H. 2020. Experimental and numerical investigation of the effect of bedding layer orientation on fracture toughness of shale rocks. *Rock Mech Rock Eng.* 53(8):3625–3635.
- Tang CA, Liu H, Lee PKK, Tsui Y, Tham LG. 2000. Numerical studies of the influence of microstructure on rock failure in uniaxial compression – Part I: effect of heterogeneity. *Int J Rock Mech Mining Sci.* 37(4):555–569.
- Tien YM, Kuo MC, Juang CH. 2006. An experimental investigation of the failure mechanism of simulated transversely isotropic rocks. *Int J Rock Mech Mining Sci.* 43(8):1163–1181.
- Vervoort A, Min K-B, Konietzky H, Cho J-W, Debecker B, Dinh Q-D, Frühwirt T, Tavallali A. 2014. Failure of transversely isotropic rock under Brazilian test conditions. *Int J Rock Mech Mining Sci.* 70:343–352.
- Wang DJ, Tang H, Shen P, Su X, Huang L. 2020a. Co-effects of bedding planes and parallel flaws on fracture evolution in anisotropic rocks. *Eng Geol.* 264:105382.
- Wang H, Liu D, Cui Z, Cheng C, Jian Z. 2016. Investigation of the fracture modes of red sandstone using XFEM and acoustic emissions. *Theor Appl Fracture Mech.* 85:283–293.
- Wang P, Cai M, Ren F. 2018. Anisotropy and directionality of tensile behaviours of a jointed rock mass subjected to numerical Brazilian tests. *Tunnelling Underground Space Technol.* 73:139–153.
- Wang W, Zhao Y, Teng T, Zhang C, Jiao Z. 2020b. Influence of bedding planes on Mode I and mixed-Mode (I–II) dynamic fracture toughness of coal: analysis of experiments. *Rock Mech Rock Eng.* 54(1):173–189.
- Wang YY, Gong B, Tang, CA. 2021. Numerical investigation on fracture mechanisms and energy evolution characteristics of columnar jointed basalts with different model boundaries and confining pressures. *Front Earth Sci.* 9:763801.
- Wang YY, Gong B, Tang CA, Zhao T. 2022a. Numerical study on size effect and anisotropy of columnar jointed basalts under uniaxial compression. *Bull Eng Geol Environ.* 81(1):41.

- Wang YY, Gong B, Tang CA. 2022b. Numerical investigation on anisotropy and shape effect of mechanical properties of columnar jointed basalts containing transverse joints. *Rock Mech Rock Eng.* <https://doi.org/10.1007/s00603-022-03018-z>.
- Wang Z, Yang S, Tang Y. 2020c. Mechanical behavior of different sedimentary rocks in the Brazilian test. *Bull Eng Geol Environ.* 79(10):5415–5432.
- Weibull W. 1951. A statistical distribution function of wide applicability. *Trans ASME, J Appl Mech.* 103(730):293–297.
- Wu Z, Lou Y, Yin S, Wang A, Liu H, Sun W, Zuo Y, Chen B. 2020. Acoustic and fractal analyses of the mechanical properties and fracture modes of bedding-containing shale under different seepage pressures. *Energy Sci Eng.* 8(10):3638–3656.
- Wu Z, Zuo Y, Wang S, Yi T, Chen S, Yu Q, Li W, Sunwen J, Xu Y, Wang R, et al. 2016. Numerical simulation and fractal analysis of mesoscopic scale failure in shale using digital images. *J Petrol Sci Eng.* 145:592–599.
- Xu G, He C, Chen Z, Su A. 2018. Transverse isotropy of phyllite under Brazilian tests: laboratory testing and numerical simulations. *Rock Mech Rock Eng.* 51(4):1111–1135.
- Xu G, He C, Yan J, Ma G. 2019. A new transversely isotropic nonlinear creep model for layered phyllite and its application. *Bull Eng Geol Environ.* 78(7):5387–5408. <https://doi.org/10.1007/s10064-019-01462-w>.
- Yu CY, Gong B, Wu N, Xu PL, Bao, X, K. 2022. Simulation of the fracturing process of inclusions embedded in rock matrix under compression. *Appl Sci.* 12(16):8041.
- Yu Z, Zhu S, Wu Y, Yu H. 2020. Study on the structural characteristics of the overburden under thick loose layer and thin-bed rock for safety of mining coal seam. *Environ Earth Sci.* 9(1):79.
- Zhang N, Yang C, Shi X, Wang T, Yin H, Daemen JJK. 2018. Analysis of mechanical and permeability properties of mudstone interlayers around a strategic petroleum reserve cavern in bedded rock salt. *Int J Rock Mech Mining Sci.* 112:1–10.
- Zhang QY, Duan K, Jiao YY, Xiang W. 2017. Physical model test and numerical simulation for the stability analysis of deep gas storage cavern group located in bedded rock salt formation. *Int J Rock Mech Mining Sci.* 94:43–54.
- Zhang Z, Jiang D, Liu W, Chen J, Li E, Fan J, Xie K. 2019. Study on the mechanism of roof collapse and leakage of horizontal cavern in thinly bedded salt rocks. *Environ Earth Sci.* 78(10):292. <https://doi.org/10.1007/s12665-019-8292-2>.
- Zhu WC, Tang CA. 2006. Numerical simulation of Brazilian disk rock failure under static and dynamic loading. *Int J Rock Mech Mining Sci.* 43(2):236–252.